The edge of galaxy formation – II. Evolution of Milky Way satellite analogues after infall

Jonas Frings, Andrea Macciò, Tobias Buck, Camilla Penzo, Aaron Dutton, Marvin Blank, Aura Obreja

▶ **To cite this version:**

Jonas Frings, Andrea Macciò, Tobias Buck, Camilla Penzo, Aaron Dutton, et al.. The edge of galaxy formation – II. Evolution of Milky Way satellite analogues after infall. Monthly Notices of the Royal Astronomical Society, 2017, 472 (3), pp.3378-3389. 10.1093/mnras/stx2171 . hal-02152459

HAL Id: hal-02152459
https://hal.science/hal-02152459

Submitted on 11 Jan 2021

HAL is a multi-disciplinary open access archive for the deposit and dissemination of scientific research documents, whether they are published or not. The documents may come from teaching and research institutions in France or abroad, or from public or private research centers.

L'archive ouverte pluridisciplinaire **HAL**, est destinée au dépôt et à la diffusion de documents scientifiques de niveau recherche, publiés ou non, émanant des établissements d'enseignement et de recherche français ou étrangers, des laboratoires publics ou privés.

Monthly Notices
of the
ROYAL ASTRONOMICAL SOCIETY

MNRAS **472,** 3378–3389 (2017)
Advance Access publication 2017 August 23

doi:10.1093/mnras/stx2171

The edge of galaxy formation – II. Evolution of Milky Way satellite analogues after infall

Jonas Frings,[1,2★] Andrea Macciò,[1,3] Tobias Buck,[1] Camilla Penzo,[1,4] Aaron Dutton,[3] Marvin Blank[3,5] and Aura Obreja[3,6]

[1]*Max-Planck-Institut für Astronomie, Königstuhl 17, D-69117 Heidelberg, Germany*
[2]*Astronomisches Recheninstitut, Zentrum für Astronomie der Universität Heidelberg, Philosophenweg 12, D-69120 Heidelberg, Germany*
[3]*New York University Abu Dhabi, PO Box 129188, Abu Dhabi, United Arab Emirates*
[4]*Laboratoire Univers et Théories, UMR 8102 CNRS, Observatoire de Paris, Université Paris Diderot, 5 Place Jules Janssen, F-92190 Meudon, France*
[5]*Institut für Theoretische Physik und Astrophysik, Christian-Albrechts-Universität zu Kiel, Leibnizstr. 15, D-24118 Kiel, Germany*
[6]*Universitäts-Sternwarte, Ludwig-Maximilians-Universität München, Scheinerstr. 1, D-81679 München, Germany*

Accepted 2017 August 18. Received 2017 August 18; in original form 2017 July 4

ABSTRACT

In the first paper, we presented 27 hydrodynamical cosmological simulations of galaxies with total masses between 5×10^8 and 10^{10} $M_\odot$. In this second paper, we use a subset of these cosmological simulations as initial conditions (ICs) for more than 40 hydrodynamical simulations of satellite and host galaxy interaction. Our cosmological ICs seem to suggest that galaxies on these mass scales have very little rotational support and are velocity dispersion (σ) dominated. Accretion and environmental effects increase the scatter in the galaxy scaling relations (e.g. size–velocity dispersion) in very good agreement with observations. Star formation is substantially quenched after accretion. Mass removal due to tidal forces has several effects: it creates a very flat stellar velocity dispersion profile, and it reduces the dark matter content at all scales (even in the centre), which in turn lowers the stellar velocity on scales around 0.5 kpc even when the galaxy does not lose stellar mass. Satellites which start with a cored dark matter profile are more prone to either be destroyed or to end up in a very dark matter poor galaxy. Finally, we found that tidal effects always increase the 'cuspyness' of the dark matter profile, even for haloes that infall with a core.

Key words: methods: numerical – galaxies: formation – galaxies: kinematics and dynamics – dark matter – cosmology: theory.

1 INTRODUCTION

The current model for the formation and evolution of the Universe predicts a hierarchical assembly of collapsed structures, with small, low-mass dark matter haloes forming first and then subsequently merging to form more massive structures (White & Rees 1978; Blumenthal et al. 1984). In such a picture, the baryonic component (i.e. the gas) will initially fall into the potential wells created by the dark matter haloes; then it will begin to efficiently cool in the centre of the overdensity, and eventually lead to the formation of stars and galaxies.

In the so-called standard model for cosmology, gravity is described by general relativity under the presence of a cosmological constant Λ (Riess et al. 1998; Perlmutter et al. 1999) and the matter component is dominated by cold dark matter (CDM; Peebles 1984). While on large scales (>Mpc), this model is very successful in predicting the observed structure of the Universe, it has been often claimed to have some issues in reproducing observations concerning the low-mass end of the galaxy population. Those challenges of the ΛCDM model on small scales became known as the missing satellites problem (Moore 1994; Klypin et al. 1999), the cusp-core tension (Flores & Primack 1994; Moore 1994; Oh et al. 2015) and the too-big-to-fail problem (Boylan-Kolchin et al. 2011). Several of these issues arise in local galaxies and mostly in the satellites around the Milky Way, so investigating the low-mass end (the edge) of galaxy formation, i.e. galaxies with stellar masses below $\approx 10^7$ $M_\odot$, can provide very important insights into the validity of our current cosmological model.

However, the physics involved in the process of structure formation becomes more and more complicated when going from large scales, which can be well described just by gravity, to small scales where baryonic effects like gas cooling, star formation and feedback play major roles. It has been pointed out that most if not all of the

★ E-mail: frings@mpia.de

© 2017 The Authors
Published by Oxford University Press on behalf of the Royal Astronomical Society

Downloaded from https://academic.oup.com/mnras/article/472/3/3378/4093087 by guest on 10 January 2021

failures of ΛCDM can be alleviated when pure *N*-body simulations are replaced by more sophisticated hydrodynamical simulations which include all baryonic effects mentioned above (Dutton et al. 2016).

Hydrodynamical simulations usually divide into cosmological volume simulations (Vogelsberger et al. 2014a; Schaye et al. 2015; Sawala et al. 2016; Grand et al. 2017) and zoom-in simulations of single objects (Macciò et al. 2012a; Aumer et al. 2013; Stinson et al. 2013; Hopkins et al. 2014; Marinacci, Pakmor & Springel 2014; Wang et al. 2015; Dutton et al. 2016; Wetzel et al. 2016). Nowadays, it is possible to achieve resolutions of few million particles per object and with a set of different zoom-in simulations the whole mass spectrum of galaxy formation can be covered (Chan et al. 2015; Wang et al. 2015). On the other hand, interacting systems like the Milky Way and its satellite galaxies, which differ by a factor 10^4 in mass, cannot be easily simulated; in fact to achieve a sufficient resolution in the satellite ($\approx 10^6$ particles) one would end up with 10^{10} particles in the Milky Way halo, which is far from manageable even for modern supercomputers. For comparison, the simulation with the best mass resolution of the Milky Way system, the Latte project (Wetzel et al. 2016), has a total of a few 10^7 particles.

To overcome this issue, different approaches have been suggested in the literature. The majority of studies have been made using modelled (pre-cooked) galaxies and then studying their evolution on (several) orbits around their host in isolated simulations (Kazantzidis et al. 2004b; Mayer et al. 2006; Kang & van den Bosch 2008; D'Onghia et al. 2009; Chang, Macciò & Kang 2013; Kazantzidis et al. 2017). While this may be a good approach to investigate the second part of the evolution of a satellite galaxy, the interaction of the satellite with its host, the use of these modelled galaxies neglects the first part of the life of satellite: its formation and evolution before the accretion on to the host.

In this series of papers, we have decided to use a new approach, which aims to combine the insights from full cosmological hydrodynamical simulations with the very high resolution attainable in simulations of binary galaxy interactions. Namely we use cosmological hydrodynamic simulations to produce realistic initial conditions for the isolated simulation of satellite–host interaction. In the first paper (Macciò et al. 2017) (from now on referred to as Paper I), we have introduced our cosmological simulations and presented a detailed analysis of the properties of our simulated galaxies *before* the accretion. In this second paper (Paper II), we study the evolution of these galaxies after they have been exposed to the environmental effects of their central object. Our final goal is to study the effects of accretion and environment on realistic satellite galaxies.

In this paper, we start in Section 2 with a short description of the simulation code, how the isolated accretion simulations are set up and how we model different physical effects. In Section 3, we present the results of our simulations, focusing on mass-losses, scaling relations, stellar kinematics and dark matter structure. Finally, in Section 4, we present our discussion and conclusion on the environmental effects on realistic satellite galaxies in a Milky Way mass halo.

2 SIMULATIONS

2.1 Cosmological simulations

We use a subsample of seven simulations of the dwarf galaxy sample introduced in Paper I. The original sample contains 27 cosmological zoom-in simulations of central haloes in the mass range of $5 \times 10^8 < M_{\rm dark}/{\rm M}_\odot < 2 \times 10^{10}$ of which 19 form a galaxy in their centre. The cosmological simulations were run using the smoothed particle hydrodynamics code GASOLINE (Wadsley, Stadel & Quinn 2004) until redshift $z = 1$ in a ΛCDM cosmology using the *WMAP* 7 set of cosmological parameters (Komatsu et al. 2011): Hubble parameter $H_0 = 70.2$ km s^{-1} Mpc^{-1}, matter density $\Omega_{\rm m} = 0.2748$, dark energy density $\Omega_\Lambda = 1 - \Omega_{\rm m} - \Omega_{\rm r} = 0.7252$, baryon density $\Omega_{\rm b} = 0.045\,72$, normalization of the power spectrum $\sigma_8 = 0.816$, slope of the initial power spectrum $n = 0.968$.

Table 1. Virial dark matter mass, stellar mass, virial radius (defined by an overdensity of 200 $\rho_{\rm crit}$) and dark matter particle mass of the selected subsample of simulations. For all simulations, the gravitational softening for the dark matter, stellar and gas particles are $\varepsilon_{\rm DM} = 31$ pc and $\varepsilon_{\rm gas} = \varepsilon_{\rm star} = 14$ pc, respectively.

Name	$M_{\rm DM}[{\rm M}_\odot]$	$M_{\rm star}[{\rm M}_\odot]$	r_{200}[kpc]	$N_{\rm star}$	$m_{\rm DM}[{\rm M}_\odot]$
satI	1.02e+10	8.97e+06	31.34	81629	1.36e+03
satII	5.52e+09	1.81e+06	25.65	16822	1.36e+03
satIII	5.61e+09	1.20e+06	25.60	6902	2.02e+03
satIV	2.92e+09	5.46e+05	20.65	5202	1.36e+03
satV	4.49e+08	4.25e+04	10.97	408	1.36e+03
darkI	3.04e+09	0	20.93	0	2.02e+03
darkII	2.81e+09	0	20.32	0	1.36e+03

The code set-up was the same as for the MaGICC project (Stinson et al. 2013; Kannan et al. 2014; Penzo et al. 2014) and included metal cooling, chemical enrichment, star formation and feedback from supernovae (SNe) and massive stars (the so-called early stellar feedback). The density threshold for star formation is set to 60 cm^{-3} which represents the mass of a smoothing kernel (32 particles) in a sphere of radius of the softening (see Wang et al. 2015, for more details), while the star formation efficiency is set to $c_\star = 0.1$. The cooling function includes the contribution of metals as described in Shen, Wadsley & Stinson (2010) and we also include photoionization and heating from the ultraviolet background following Haardt & Madau (2012) and Compton cooling. The SN feedback relies on the blast-wave recipe described in Stinson et al. (2006). Finally, we identified the haloes using the amiga halo finder (AHF[1]) (Knollmann & Knebe 2011).

The mass resolution of the zoom-in region of the simulations is shown in Table 1. Gas particles have an initial mass of $m_{\rm gas,\,init} = f_{\rm bar} \times m_{\rm DM}$ while stellar particles start with initial masses $m_{\rm star,init} = \frac{1}{3} m_{\rm gas,init}$, where $f_{\rm bar} = \frac{\Omega_{\rm b}}{\Omega_{\rm dark}}$ is the cosmic baryon fraction.

2.2 Satellite initial conditions

Starting from the redshift $z = 1$ snapshots of the cosmological simulations described in Section 2.1, we cut out seven haloes and their surrounding structures up to a distance of four virial radii from their centre (for the virial radius, we used the region enclosing a density equal to 200 times $\rho_{\rm crit}$, where $\rho_{\rm crit}$ is the cosmic critical matter density). These cut-out regions were then transformed from cosmological (i.e. expanding) coordinates to physical ones and used as initial conditions for our subsequent accretion simulations. Table 1 contains the main parameters of our selected haloes, the name *sat* is used for haloes which contained stars at the starting redshift ($z = 1$) while we reserve the name *dark* for haloes without stars. As a first step, we run all the haloes (dark and luminous) 'in isolation' from

[1] http://popia.ft.uam.es/AMIGA

Downloaded from https://academic.oup.com/mnras/article/472/3/3378/4093087 by guest on 10 January 2021

Table 2. Compilation of the different orbit scenarios with their initial velocity, pericentre distance and orbit inclination with respect to the host galaxy disc. All orbit initiate at the coordinates $x = 210$ kpc, $y = z = 0$. The colour indicates the colour coding in Fig. 1.

Name	(v_x, v_y, v_z) $[v_{200}]$	$\tau_{\rm ram}$ [Gyr]	$r_{\rm min}$ [kpc]	ϑ [deg]
orbitI	$(-0.45, 0.3, 0)$	1.5	25.52	0
orbitII	$(-0.45, 0, 0.3)$	1.5	25.46	90
orbitIII	$(-0.2, 0.2, 0.2)$	1.5	25.26	45
orbitIV	$(-0.5, 0, 0.1)$	1.4	7.94	90
orbitV	$(-0.5, 0.1, 0)$	1.4	7.2	0
radial	$(-0.5, 0, 0)$	1.3	–	0

$z = 1$ to 0, meaning we evolved them without the presence of the central halo, in order to have a baseline for the evolution of our galaxies; we will refer to this set of simulations as the *isolated* runs.

2.3 Central object parametrization

We used two different models for the parametrization of the central object. At first, we described it as an analytical potential consisting of the superposition of two distinct potentials for the dark matter and the stellar disc. For the dark matter halo we used a Navarro–Frenk–White (NFW) potential (Navarro, Frenk & White 1996) with a mass $M_{200} = 1 \times 10^{12}$ M$_\odot$, a concentration parameter $c = 10$ (Dutton & Macciò 2014) and a virial radius $r_{200} = 210$ kpc. For the stellar body, we used a Miyamoto & Nagai potential (Miyamoto & Nagai 1975) with a disc mass $M_{\rm disc} = 5 \times 10^{10}$ M$_\odot$, disc scalelength $R_{\rm disc} = 3.0$ kpc and height $h_{\rm disc} = 0.3$ kpc. The disc is aligned with the $x - y$ plane of the simulation.

The use of an analytical potential makes the simulation faster but misses one possible important ingredient: dynamical friction. In order to estimate its effect, we also used a live halo (i.e. made with particles) without a disc component.

To construct the (central) galaxy model, we apply the method described in Springel, Di Matteo & Hernquist (2005) and in Moster, Macciò & Somerville (2014). The halo is described by an NFW density profile with the same parameters used for our analytical potential (a virial radius of $r_{200} = 210$ kpc, a virial mass of $M_{200} \approx 1 \times 10^{12}$ M$_\odot$ and a concentration parameter of $c = 10$). We used two resolution levels for this live halo with 10^5 and 10^7 particles, respectively. Runs performed with the live halo are discussed in the next section.

2.4 Orbits

We select six different orbits and run the simulations until redshift $z = 0$.

All orbits start at the virial radius at the coordinates $(x, y, z) = (210.0,\ 0,\ 0)$ kpc but they differ in the initial velocity of the satellite and in the angle between the plane of the orbit and the stellar disc of the host halo. The parameters of all orbits are summarized in Table 2, where we have ordered the six orbits by their 'disruptiveness', i.e. *orbitI* is the most gentle orbit, causing the least deviations from the isolated run (for example in mass-loss) while *orbitV* provides the most violent interaction between the satellite and the central object, with the exception of the complete radial infall. The pericentre distance is shown only for *satV*. We want to point out that compared to the orbits of surviving Milky Way satellites even *orbitI* with a pericentre of 25 kpc is quite extreme. Garrison-Kimmel et al. (2017) show that in their simulations only 5 per cent of the surviving satellites around Milky Way mass galaxies have orbital pericentres

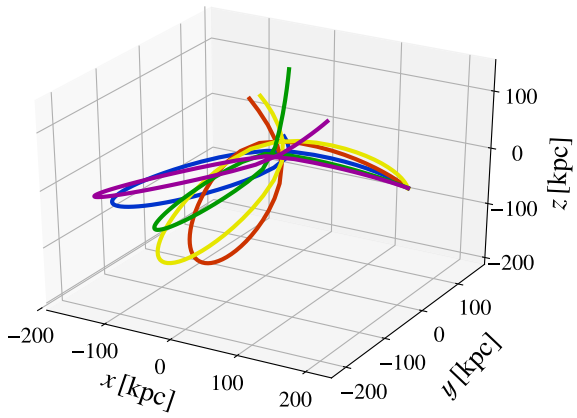

Figure 1. Visualization of the orbits (*orbitI* to *orbitV*) presented in Table 2 from infall to 5.7 Gyr after infall. The colour coding is the same as in Table 2.

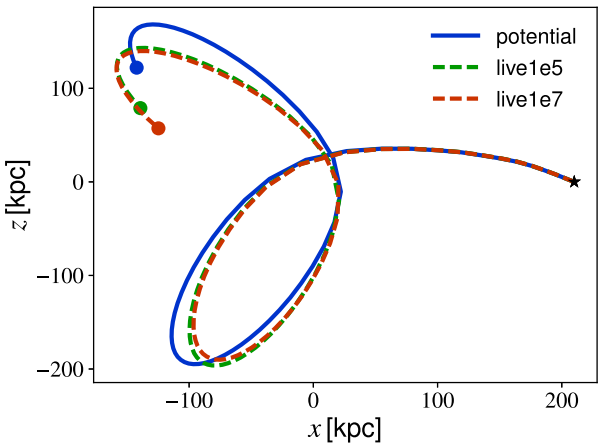

Figure 2. Projection of *orbitII* on to the $x - z$ plane comparing the evolution in an analytical potential (blue), in a live halo with 10^5 (green) and 10^7 (red) dark matter particles. A star marks the start of the orbit while the dot marks the end.

below 20 kpc. The choice for such strong orbits has been dictated by our aim to bracket the possible scenarios between unperturbed evolution (the isolation case) and strong interactions.

In Fig. 1, we show the trajectory of *satV* on the orbits from *I* to *v* from $z = 1$ to $z = 0$ (5.7 Gyr). The colours correspond to individual orbits as introduced in Table 2. The centre of each satellite is defined as the position of the maximum of the stellar (dark matter) density distribution for the luminous (dark) satellites. The position of this maximum is derived via a shrinking spheres algorithm according to Power et al. (2003).

In Fig. 2, we compare the orbit evolution of *orbitII* in the analytical potential in the live halo at two different resolution levels: 10^5 and 10^7 particles. Dynamical friction does slightly modify the orbit, but the effect is quite small and independent of the resolution of the live halo, the same result also holds for the other orbits. Since our choice of orbits has been practically random, it is fair to say that the small effect of dynamical friction is very similar to a slightly different choice of orbits, and can be then neglected in our study.

2.5 Ram pressure

Even with a live halo, our set-up is not able to take into account the effect of ram pressure between the (hot) gas in the host halo and the gas in the satellite. We therefore add an analytical recipe for

Downloaded from https://academic.oup.com/mnras/article/472/3/3378/4093087 by guest on 10 January 2021

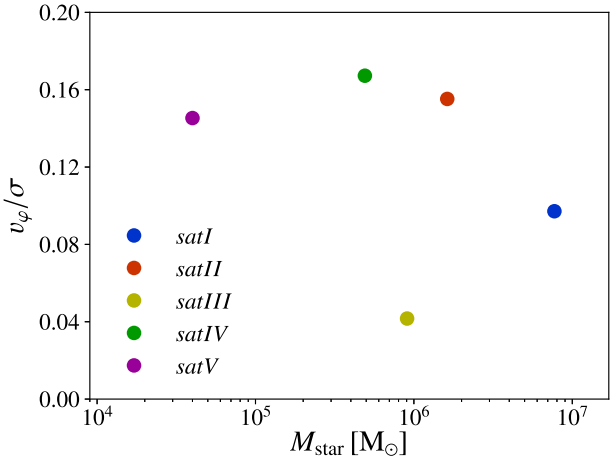

Figure 3. Amount of rotation along the axis of total stellar angular momentum of the stars compared to stellar velocity dispersion as a function of stellar mass.

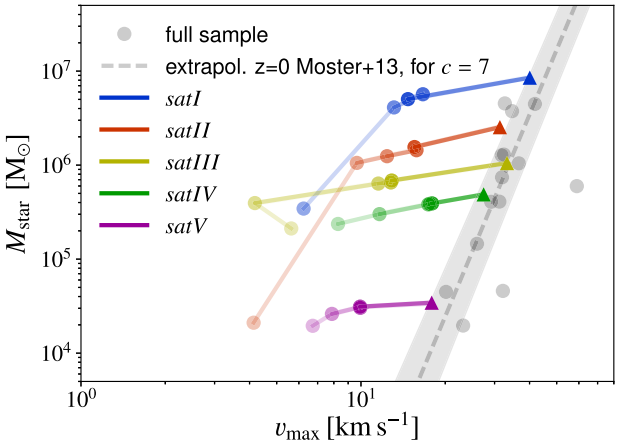

Figure 4. The stellar mass within three stellar 3D half-mass radii (at infall) as a function of the maximum circular velocity. The grey band shows the Moster relation and its errors translated to a function of $v_{\rm max}$ for a concentration of $c = 7$. Triangles denote the isolated simulations while the filled circles denote the different orbits. The more violent the orbit, the fainter is the colour of the dots.

ram pressure to our simulations. At every basic time-step (1 Myr), we remove all gas particles within the satellite which are below a certain threshold density $\rho_{\rm th}$. This density threshold evolves with time according to the following expression:

$$\rho_{\rm th}(t) = \begin{cases} \rho_{\rm max} \left[\frac{\rho_{\rm min}}{\rho_{\rm max}}\right]^{\left(1-\frac{t}{\tau_{\rm ram}}\right)^a}, & \text{for } t < \tau \\ \rho_{\rm max}, & \text{for } t > \tau \end{cases} \quad (1)$$

where $\rho_{\rm min}$ is the gas density at four virial radii; $\rho_{\rm max}$ is the gas density in the centre of the halo; $\tau_{\rm ram}$ is the gas removal time-scale (see below for more details); a is a free parameter and t denotes the runtime of the simulation.

If in equation (1), we set $\rho_{\rm th}(t = 0) = \rho_{\rm min}$ and $\rho_{\rm th}(t = \tau_{\rm ram}) = \rho_{\rm max}$, this implies that all gas will be removed (outside in) at time $t = \tau_{\rm ram}$. We fixed the value of the parameter a at 0.2, since this ensures that $\rho_{\rm th}$ follows the radial profile of the gas density. Finally, we set the gas removal time-scale $\tau_{\rm ram}$ approximately equal to a half the dynamical time-scale of the orbit, so that all gas is removed after one pericentre passage (see Table 2).

We do not expect ram pressure to be important from a dynamical point of view, since our galaxies are very strongly dark matter dominated (see Paper I), but it might be important to accelerate the galaxy quenching. On the other hand, by comparing *satIV* on *orbitII* with and without ram pressure we found no strong changes in its star formation rate, with both set-ups showing a very similar quenching behaviour compared to the isolated run.

Even if we do not see a large difference in the outcomes of the simulations with and without the ram pressure model, we still apply the ram pressure model to all simulations since it decreases the computational cost (by reducing the number of gas particles within the galaxy).

3 RESULTS

3.1 Rotational support

One main difference between our approach and previous studies in the literature is the use of cosmological simulations as initial conditions, it is then interesting to check the dynamical state of our galaxies before the infall. In Fig. 3, we show the amount of rotational support of the stellar component in the dwarf galaxies at $z = 1$. We obtain the rotational velocity v_φ by averaging the individual velocities of the stellar particles in $\boldsymbol{e}_\varphi$ direction. The unit vector $\boldsymbol{e}_\varphi$ is set as the circumferential direction with respect to the axis defined by the total stellar angular momentum of stars within the half-mass radius. The velocity dispersion σ is simply given by $\sigma = \sigma_{3D}/\sqrt{3}$, where σ_{3D} is the three-dimensional velocity dispersion of the stellar particles in the half-mass radius. As shown in Fig. 3, our galaxies show that there is not much rotational support and their structure can be described by a single isotropic component with practically no signs of a stellar disc even before infall. This is in agreement with previous studies which showed that in cosmological simulations, isolated dwarf galaxies as well as satellite galaxies at the low-mass end seem to be dispersion-supported systems (Wheeler et al. 2017).

However this is quite different from several previous works studying satellite–host interaction, which usually adopted values of $v_{\rm rot}/\sigma \approx 2$ (Kazantzidis et al. 2017) with a well-defined disc component, and then witness a 'morphological transformation' within the host halo (Łokas et al. 2010). In our case, no morphological transformation is needed since cosmological simulations seem to indicate that galaxies, on our mass scales, are already quite 'messy' and do not show the presence of a stellar disc.

3.2 Environmental effects on galaxy properties

All the satellites survive till redshift $z = 0$ on orbits from *orbitI* to *orbitV* with the exception of *satI* on *orbitV*, since in this case our centreing algorithm is not able to find a well-defined stellar (or dark matter) centre for the satellite, as it is also confirmed by a visual inspection which shows the satellite being completely destroyed. The same happens for the radial orbit scenario, in which all satellites are destroyed with no exceptions, we plan to analyse these tidal debris in a forthcoming paper. Since in this paper, we are interested in the properties of 'alive' satellites at $z = 0$, we will therefore focus on *orbitI* to *orbitV* for all our satellites but excluding *orbitV* for *satI*.

Mass-loss and abundance matching

In Fig. 4, we show the stellar mass within three half-mass radii at infall as a function of the maximum of the total circular velocity

Downloaded from https://academic.oup.com/mnras/article/472/3/3378/4093087 by guest on 10 January 2021

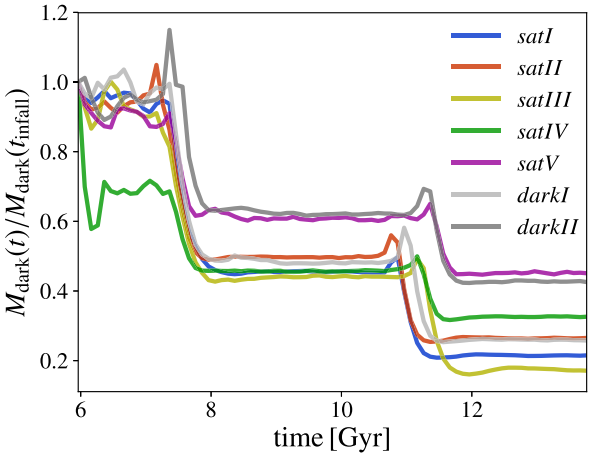

Figure 5. Evolution of the dark matter mass in terms of the dark matter mass at infall of the seven satellites on *orbitII*. Only the mass in 10 per cent of the virial radius at infall is considered.

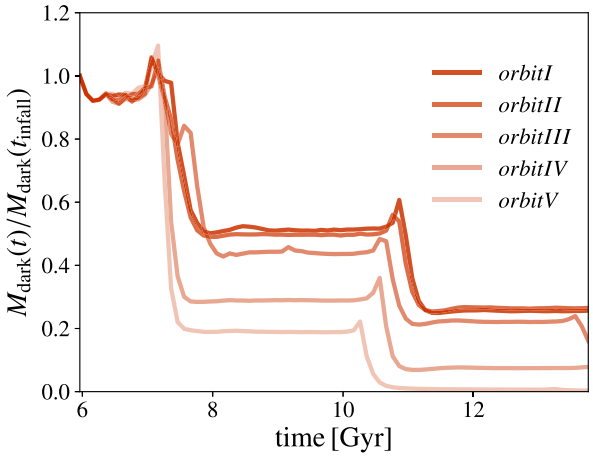

Figure 6. Evolution of the dark matter mass in terms of the dark matter mass at infall for *satII* on the five orbits. Only the mass in 10 per cent of the virial radius at infall is considered.

profile $v_{\rm max}$. The half-light radius is determined by the radius of a sphere around the centre of the satellite containing half of its stellar mass, we will refer to this measure as the 3*D* half-mass radius. The (coloured) triangles mark the results for the isolated runs at redshift zero. The (coloured) filled circles represent the runs in the disc+halo potential, same colours refer to the same satellite (they are also connected by a line to facilitate the comparison), while the strength of the colour goes from dark to faint as the orbit becomes more destructive, i.e. from orbits (*orbitI* to *orbitV*). We will use the same colour scheme in the rest of the paper. Finally, the grey circles represent the full sample of haloes presented in Paper I at $z = 1$ and are only added for comparison.

The dashed grey line shows the extrapolation to low-mass haloes of the abundance matching relation from Moster et al. (2013) and its error band. Since for satellites it is hard to define the total halo mass, we have translated this last quantity into a maximum circular velocity. This has been assuming an NFW potential for the total matter distribution with concentration $c = 7$ (which is the average concentration of our simulated haloes) and also assuming that the maximum circular velocity occurs at the radius $r = 2.16\, r_s$ (Bullock et al. 2001) where r_s is the NFW scale radius.

Our galaxies started on the abundance matching relation (grey circles, see also Paper I), and they remain there when run in isolation (coloured triangles). Then depending on the orbit, they leave the relation as a consequence of tidal stripping. For quiet orbits, they move almost parallel to the *x*-axis (i.e. with constant stellar mass), meaning that the central region of the satellite is fairly unaltered, then also for more disruptive orbits the stellar component is affected and the stellar mass can shrink up to 1 per cent of its initial value. Overall the satellites seem to perform a characteristic curve in the stellar mass versus maximum circular velocity plane due to tidal stripping.

It is interesting also to look at the time evolution of the dark matter mass near the (luminous) centre of our haloes. In Fig. 5, we show the evolution of the dark matter mass enclosed in 10 per cent of the initial (at infall) virial radius for all our satellites on the same orbit, namely *orbitII*.

Until the first pericentre passage at $t \approx 8$ Gyr, the dark matter mass is more or less stable with the exception of *satIV* in which a (sub)substructure which passed nearby the centre led to an overestimation of the initial enclosed mass. During the first pericentre passage, the satellites lose about half their inner dark matter mass. Then, we find again a quite stable period until the second pericentre passage at $t \approx 11$ Gyr, when the satellites are stripped again and left with 15–50 per cent of their initial dark matter mass at redshift $z = 0$.

The second stripping event, corresponding to the second pericentre passage, occurs in the time range 11–12 Gyr for all the satellites. The more massive satellites, however seem to experience this event earlier (shortly after 11 Gyr) than the less massive ones. This implies a sort of 'decay' of the orbital trajectory for more massive satellites even in the absence of dynamical friction. This can be ascribed to the different redistribution of energy and orbital angular momentum between stripped material and the satellite remnant. Finally in Fig. 6, we show the evolution of the dark matter mass this time for a single satellite (*satII*) on all five orbits. The fraction of dark matter remaining in the halo at redshift $z = 0$ varies from 30 per cent on *orbitI* to just a few percent on *orbitV*.

Stellar mass assembly

We now turn our attention to the luminous part of the satellites. The evolution of the stellar mass in the cosmological simulations until redshift $z = 1$ (dashed) and physical simulations (solid) is shown in Fig. 7 for the isolated run and *orbitII* (faint lines).

The stellar mass as a function of time is reconstructed from the formation times of the individual stellar particles. All stellar particles that remain within 10 per cent of the virial radius $r_{200,\,\rm infall}$ at infall at redshift $z = 0$ are considered and weighted with their initial stellar mass $m_{\rm star,\,init}$. We will use the virial radius at infall as a scale for the dark matter halo during the satellite evolution and we will refer to it just as the virial radius r_{200}. The star formation before infall has been further investigated in Macciò et al. (2017). The galaxies show various behaviours of star formation in isolation, from absence of star formation in *satV* to a starburst due to a merger with substructure in *satII*. On the orbit, however the star formation plays no or at least a minor role.

Metallicity

We present the mass-weighted stellar metallicity as a function of stellar mass enclosed in a sphere of three 2D half-mass radii in Fig. 8. Where the 2D half-mass radius is defined as the radius of a

Downloaded from https://academic.oup.com/mnras/article/472/3/3378/4093087 by guest on 10 January 2021

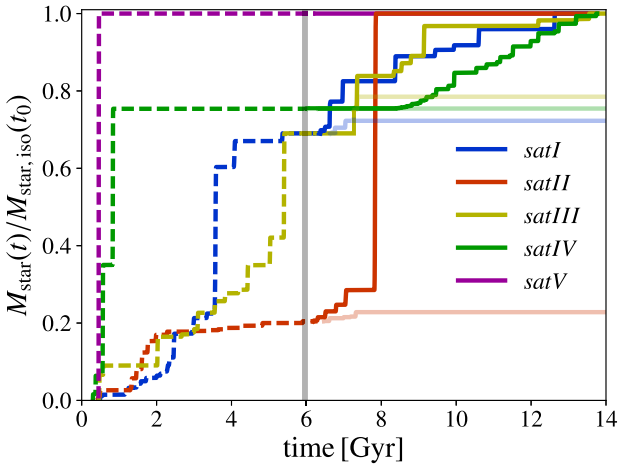

Figure 7. Evolution of the stellar mass of the five luminous satellites before (dashed) and after (solid) the infall time ($z = 1$). Isolated runs are shown with darker colours while orbits (specifically *orbitII*) are shown with fainter ones. The stellar mass is shown in terms of the stellar mass at time $z = 0$.

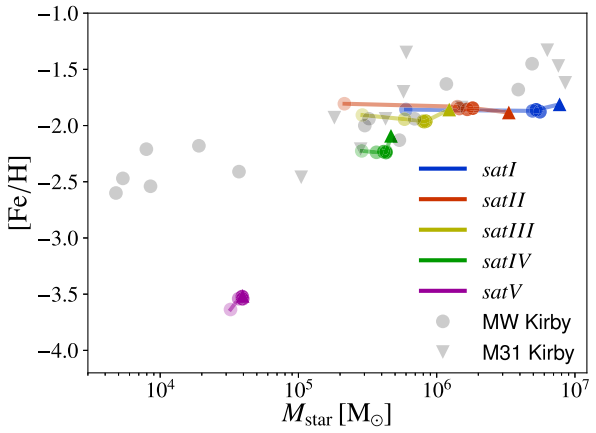

Figure 8. Metallicity as a function of the stellar mass. The coloured triangles denote the isolated simulations while the filled circles denote the different orbits. The more violent the orbit, the fainter is the colour of the dots. Observations of Milky Way and M31 satellites from Kirby et al. (2014) are shown as grey dots and triangles, respectively.

cylinder along the z-axis (our line of sight) containing half of the galaxy stellar mass.

As before the triangle marks the position of the isolated simulation, while the different coloured circles mark the results for the different orbits, with faint colours being associated with more disruptive orbits. The grey circles and triangles represent observational results for the Milky Way and the M31 galaxy, respectively. Our isolated runs nicely reproduce the observational trend from Kirby et al. (2014), with the exception of *satV*, the apparent failure of this satellite is related to the very short time-scale of star formation compared with the time-step of the simulation, which does not allow for a proper treatment of the enrichment (see Paper I for a thorough explanation of this issue).

When the satellites are exposed to the presence of a central halo, they do lose stellar mass (as expected), but they still move parallel to the relation, with an almost constant metallicity, due to the very low metal gradient in their stellar population.

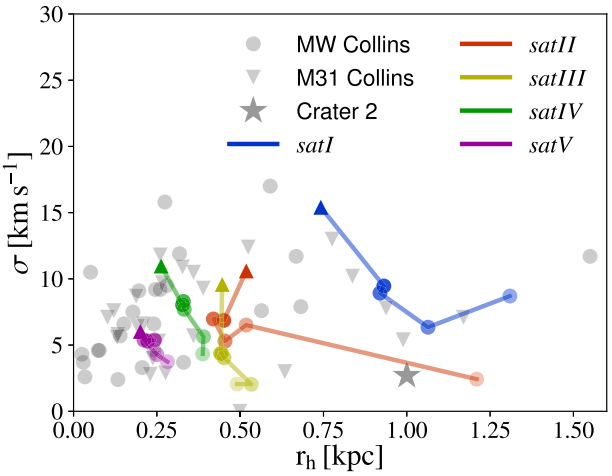

Figure 9. Projected velocity dispersion inside the stellar 2D half-mass radius as a function of the stellar 2D half-mass radius. Coloured triangles denote the isolated simulations while the filled circles denote the different orbits. The more violent the orbit, the fainter is the colour of the dots. Observations of Milky Way and M31 satellites (for references see Section 3.2) are shown as grey dots (and a star for the recently discovered satellite Crater 2) and triangles, respectively.

Stellar kinematics

The effect of accretion on to a more massive galaxy is instead clearly visible in the velocity dispersion–size relation which is shown in Fig. 9. The size ($r_{\rm h}$) is again the 2D half-mass radius already introduced above, while the velocity dispersion is the 1D dispersion along the line of sight (the z-axis in our case) computed within $r_{\rm h}$. In this plot, the observational data are represented by grey dots and triangles for Milky Way and M31 satellites, respectively. They are taken from a compilation from M.Collins (private communication) including data from Walker et al. (2009) for the Milky Way and Tollerud et al. (2012), Tollerud et al. (2013), Ho et al. (2012), Collins et al. (2013) and Martin et al. (2014) for M31 satellites. The size and dispersion measurements of the recently discovered satellite Crater 2 are taken from Caldwell et al. (2017).

Our isolated haloes (triangles) lie well within the relation as were our initial conditions (see Paper I). Stripping and tidal forces modify both the size and the velocity dispersion of the galaxies, which, depending on the orbit, at redshift zero tend to occupy the whole space covered by the observations.

It is interesting to note that simulated galaxies with larger sizes tend to have a larger deviation (both in size and dispersion) from the isolated runs, suggesting that small galaxies tend to be more resilient to tidal effects. Overall the scatter in our simulated size–dispersion velocity is in very good agreement with the observed one. Further, we want to emphasize that *satII* and *orbitV* end up with an extremely low velocity dispersion at a half-mass radius of about 1.2 kpc. This is in very good agreement with the properties of the recently discovered Crater 2 satellite (Caldwell et al. 2017). This implies that the formation of such extended and cold structures is not a challenge for the current LCDM model, which can be explained as highly perturbed objects (see also Munshi et al. 2017).

To better understand the time evolution of the stellar kinematics in our satellites, in Fig. 10 we show the radial profile of the three-dimensional stellar velocity dispersion on *orbitII* at three different times: at infall and after 3 and 7.8 Gyr (corresponding to redshift $z = 0$). Here, we only consider *satI* to *satIV* because *satV* does not have sufficient stellar particles to resolve the kinematics properly

Downloaded from https://academic.oup.com/mnras/article/472/3/3378/4093087 by guest on 10 January 2021

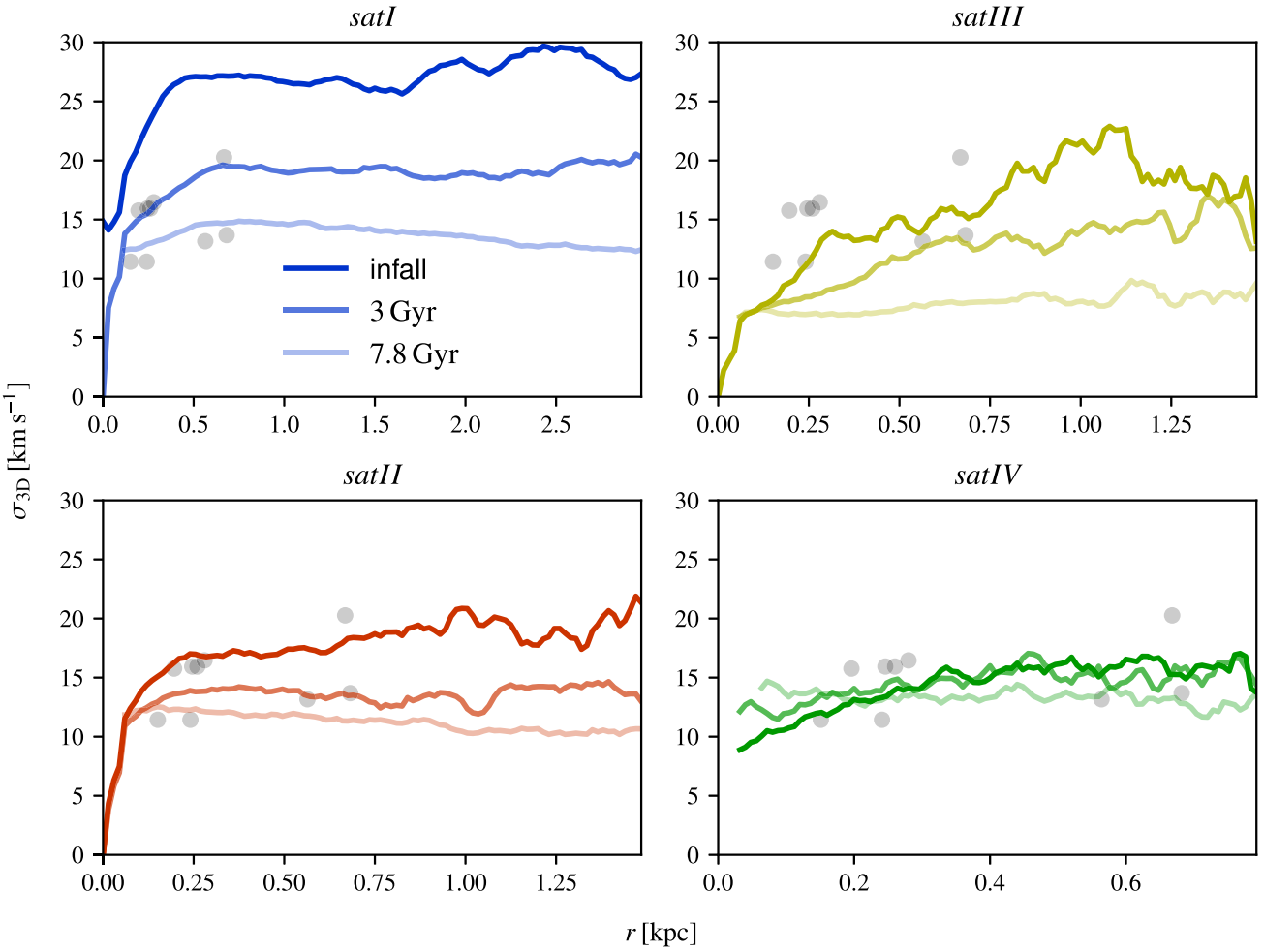

Figure 10. Three-dimensional velocity dispersion of the stellar particles on *orbitII* evaluated at infall (solid), 3 Gyr and 7.8 Gyr ($z \approx 0$) (faint, solid). Grey points denote line-of-sight velocity dispersion measurements from Walker et al. (2009) of the nine most massive Milky Way satellites rescaled by a factor of $\sqrt{3}$ (Wolf et al. 2010).

(see Table 1). In the same plot, we also show as reference (grey circles) the line-of-sight velocity dispersion measurements for the nine most massive Milky Way satellites at the half-light radius from Walker et al. (2009) rescaled by a factor of $\sqrt{3}$ (see Wolf et al. 2010)). As time goes by, the mass (DM+stellar) loss causes an overall decrease of stellar velocity dispersion, which also tends to become more isothermal, with a very flat distribution (see for example the case for *satIII*) at redshift zero. We ascribe this effect to the particle phase space mixing due to tidal effects, which seems to 'thermalize' the galaxy.

Another interesting (and measurable) quantity to look at is the circular velocity, defined as $v_{\rm circ} = \sqrt{\frac{GM(<r)}{r}}$, where $M(< r)$ is the total mass enclosed in a sphere with radius r around the centre. In Fig. 11, we show the final ($z = 0$) circular velocity radial profile for all our seven satellites and for different orbits. In each panel, the black line represents the isolated run, while the coloured lines are the orbit runs, with, as before, fainter colours for more disruptive orbits. We also show, as in the previous figures, the observations of the nine most massive Milky Way satellites as an orientation (data from Walker et al. 2009). As already noted in previous studies, circular velocity profiles can be significantly lowered in the inner few hundred parsecs, even without losing a large amount of mass on these scales (see Fig. 4). The profiles also tend to evolve in a sort of self-similar way, preserving their initial shape, with the exception of the most extreme orbit.

3.3 Evolution of the dark matter profile

We now turn our attention to the dark (matter) component of our satellites. In Fig. 12, we show the redshift zero dark matter distribution for all our galaxies in the various runs at redshift $z = 0$, as before the black line represents the isolation run, while the coloured lines are for the different orbits. The profiles are shown from twice the gravitational dark matter softening to the virial radius at infall (the exceptions are satellites *satI*, *satII* and *satIII* on the most extreme orbit, since they end up with a very low dark matter content at $z = 0$ and which pushes the convergence radius to larger scales). As expected, the tidal stripping due to the central potential is stronger in the outer parts of the profile, which depart more from the isolation case. On the other hand, the stripping does not happen in an 'onion-like' fashion, with the outer part being progressively removed while the centre remains unaltered. On the contrary, the whole profile reacts to the stripping and the central density is also lowered even on the mildest orbits. This global reaction can be

Downloaded from https://academic.oup.com/mnras/article/472/3/3378/4093087 by guest on 10 January 2021

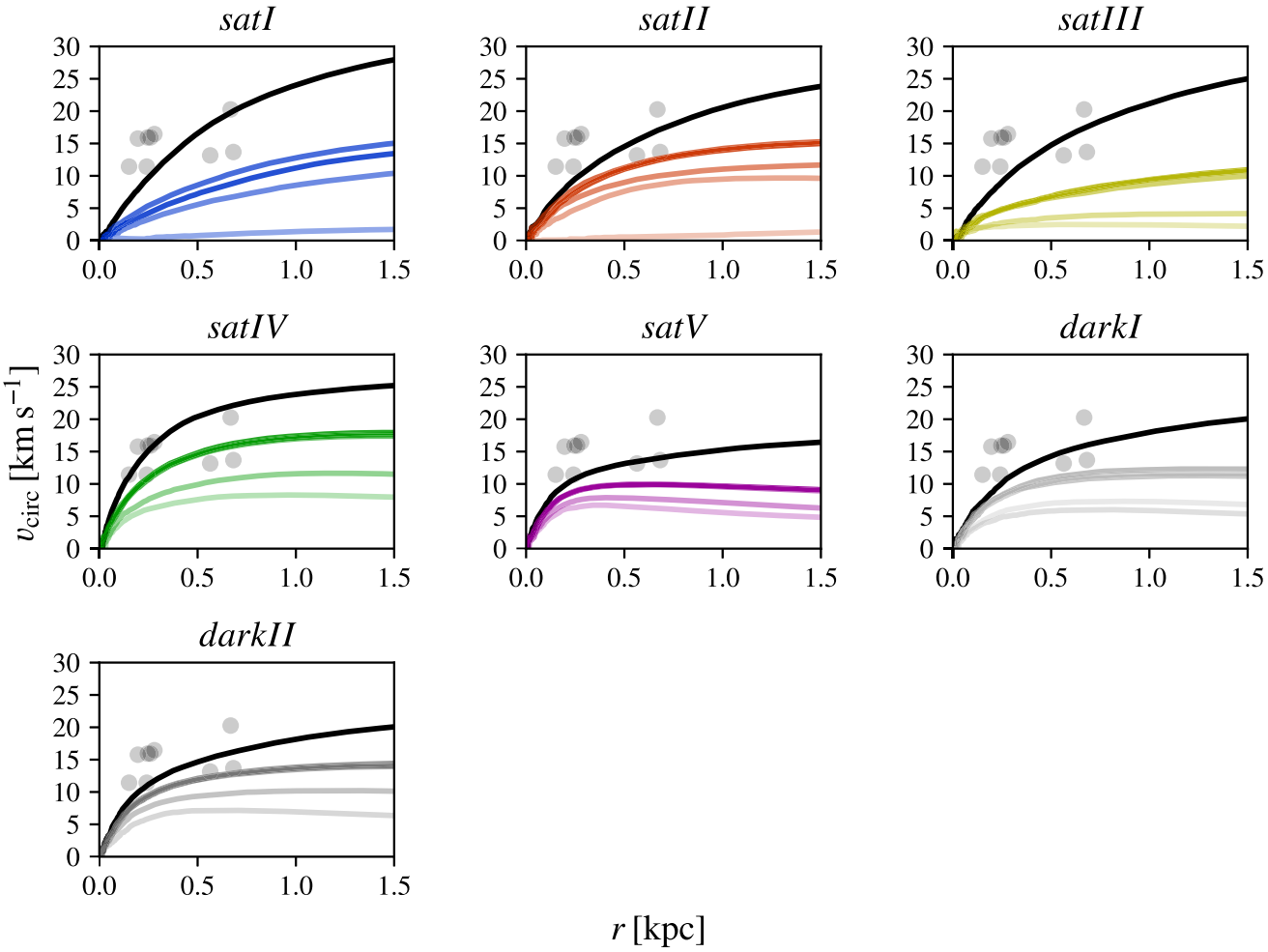

Figure 11. Circular velocity profiles for the five luminous satellites for the isolated run (black) and the orbits (colour coding as before). The more violent the orbit, the fainter is the line colour. Grey points denote line-of-sight velocity dispersion measurements from Walker et al. (2009) of the nine most massive Milky Way satellites rescaled by a factor of $\sqrt{3}$ (Wolf et al. 2010).

ascribed to the typical box orbits of dark matter particles (e.g. Bryan et al. 2012), which allow particles in the centre at a given time-step, to spend quite some time in the outskirts of the halo at a subsequent time, and hence are prone to be stripped.

As already described in Paper I, some of our satellites (*satI, satII, satIII* as shown by the isolation runs) start with a cored dark matter profile (or at least a profile with a shallower slope than NFW), this is due to the fact that for those satellites, the star formation rate is vigorous enough to create large gas outflows, which in turn flatten the dark matter profile (Read & Gilmore 2005; Macciò et al. 2012b; Pontzen & Governato 2012; Di Cintio et al. 2014; Oñorbe et al. 2015). Fig. 12 seems to suggest a steepening of the profile during its evolution. To better look into this possibility we plot in Fig. 13, the inner logarithmic dark matter density slope α as a function of stellar mass. The slope α is computed between 1 and 2 per cent of the initial (at infall) virial radius, following Tollet et al. (2016) and Paper I; the triangles mark the isolation runs, while the circles represent the different orbits, finally the stellar mass for the two dark haloes has been arbitrarily set.

No matter if the halo contained stars or not, or whether it starts with a flattened profile (blue and yellow symbols) or with a cuspy one (green symbols), in all cases the effect of accretion is to steepen the dark matter profile. It is important to notice that the profile steepening is not due to a contraction of the halo but it is due to a slightly stronger mass removal in the outer regions of the halo with respect to its very centre.

In Fig. 12, we do not show the final density profile slope for *satI* (blue), *satII* (red) and *satIII* (yellow) for the most extreme orbit. This is because at $z = 0$ these satellites do not have a clear dark matter centre to build the profile. It is nevertheless interesting to look at the evolution of the dark matter profile as a function of time before the satellite disruption. This is shown in Fig. 14 where we present the difference of the density slope α w.r.t. to the isolation case as a function of time: the plots show *satI* (blue line), *satII* (red line) and *satIII* (yellow line) on *orbitIV* (for *satI*) and *orbitV* (for *satII* and *satIII*), respectively, and the profile slopes are averaged over five time-steps to reduce the noise. It is evident that the steepening of the profile is present even for satellites that are completely shredded apart by tidal forces.

When the results of Paper I and this work are combined, they imply that the observational discovery of a dark matter core in one of the low-mass satellites of our own Galaxy will strongly challenge the predictions of the ΛCDM model. It will be very difficult to explain such dark matter core invoking the effect of baryons (Paper I

Downloaded from https://academic.oup.com/mnras/article/472/3/3378/4093087 by guest on 10 January 2021

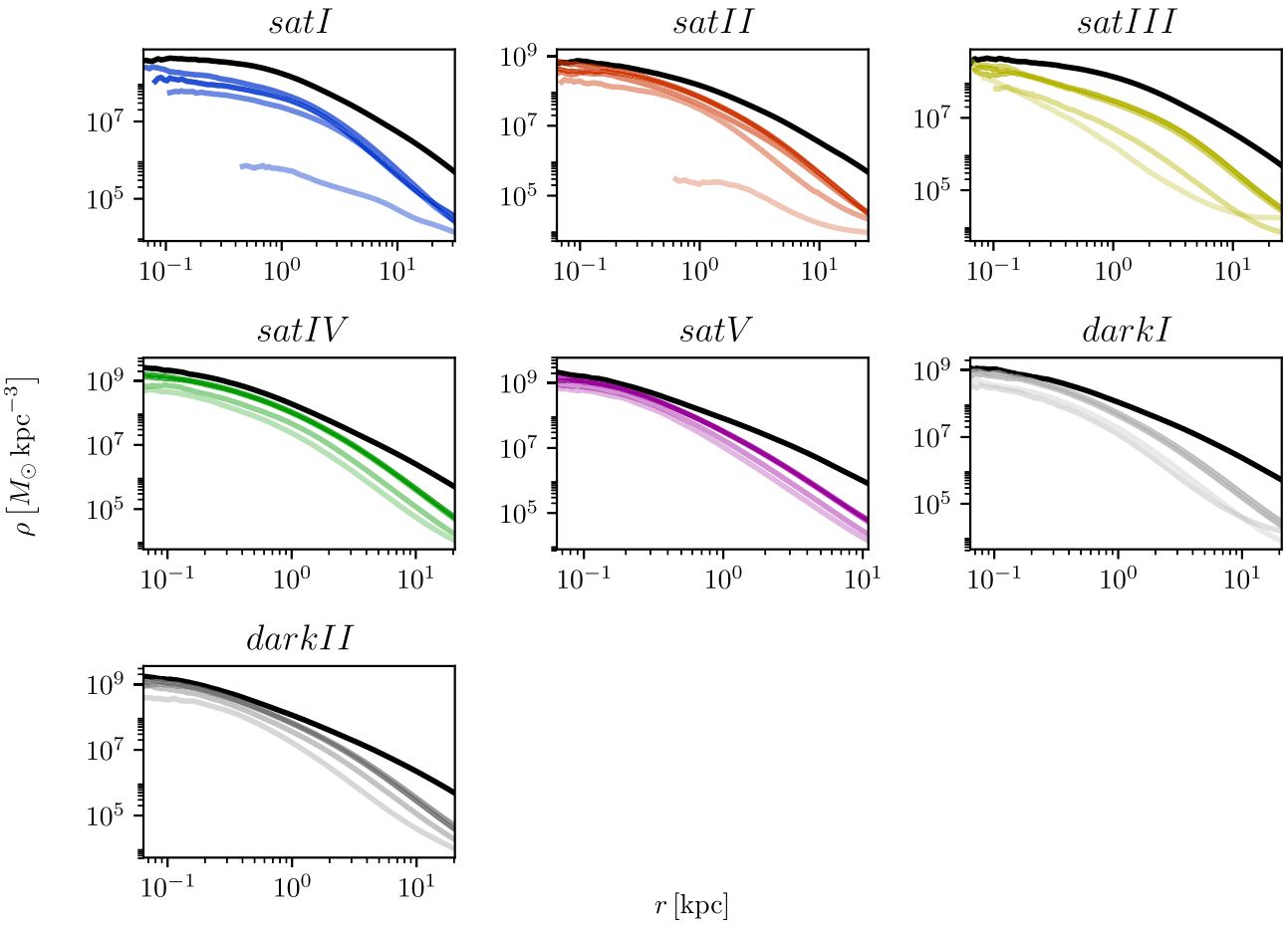

Figure 12. Dark matter density profile of all the satellites in isolation (black) and on the orbits (colour coding as before) at redshift $z = 0$. The more violent the orbit, the fainter is the line colour. The profiles are shown from twice the softening length up to the virial radius at infall.

and triangles in Fig. 13) or the effect of environment and accretion (again Fig. 13). The discovery of a flat dark matter distribution will then be an indication of a different nature for dark matter: warm (but see Macciò et al. 2012a), self-interacting (Vogelsberger et al. 2014b; Elbert et al. 2015) or even more exotic models (e.g. Macciò et al. 2015).

3.4 Central dark matter density slope and satellite survival

Previous works studying environmental effects on satellite galaxies (e.g. Kazantzidis et al. 2004a; Peñarrubia et al. 2010, and references therein) have shown that satellites with cored dark matter density profiles are more easily stripped and disrupted than cuspy ones. The results shown in Fig. 13 seemed to confirm such a correlation also in our cosmologically based simulations, but we want to be more quantitative.

In Fig. 15, we show the ratio of the dark matter enclosed within three half-mass radii for the different satellites on the different orbits with respect to the isolated case as a function of the initial (at infall) density profile slope at redshift $z = 0$. It is quite evident that on every orbit, cuspy satellites like *satV* ($\alpha_{\rm infall} = -1.5$) are able to retain a larger fraction of their initial mass than cored ($\alpha_{\rm infall} > -1.0$) satellites like *satI* and *satIII*. These cored satellites lose more than 70 per cent of their initial (dark) mass even on the more gentle orbit (darker colours) and up to almost 100 per cent on the most extreme ones (fainter colours).

The different initial dark matter density slope also affects the stellar mass-loss, since the dark matter acts as shield for the stars. In Fig. 16, we plot the mass-loss as defined in Fig. 15 as function of the initial dark matter profile density slope but this time for stars and dark matter. In order to avoid a too crowded plot, we only show results for *orbitIV*, which is the most disruptive orbit for which all five satellites still have a well-defined centre.

In general stars are more resilient to tidal forces than dark matter, and this is due to their smaller spatial extent and larger stellar density; for example *satIII* is able to retain 40 per cent of its stars while it is practically totally stripped of dark matter. Nevertheless there is still a correlation between the stellar mass-loss and the initial dark matter slope. An exception to this relation seems to be given by *satI*, which has a very strong mass-loss both in the stellar and dark matter components despite having a similar $\alpha_{\rm infall}$ as *satIII*. This is due to the different slope for the *stellar* density profiles between *satI* and *satIII*, while the first satellite has a slope of -1.80 (again evaluated between 1 and 2 per cent of the virial radius), the stellar slope for *satIII* (and all the other satellites) it is close to -3.0. This difference in stellar slope is most likely related to a major merger event that occurred for *satI* shortly before redshift one and strongly reshuffled the stellar particle orbits.

Downloaded from https://academic.oup.com/mnras/article/472/3/3378/4093087 by guest on 10 January 2021

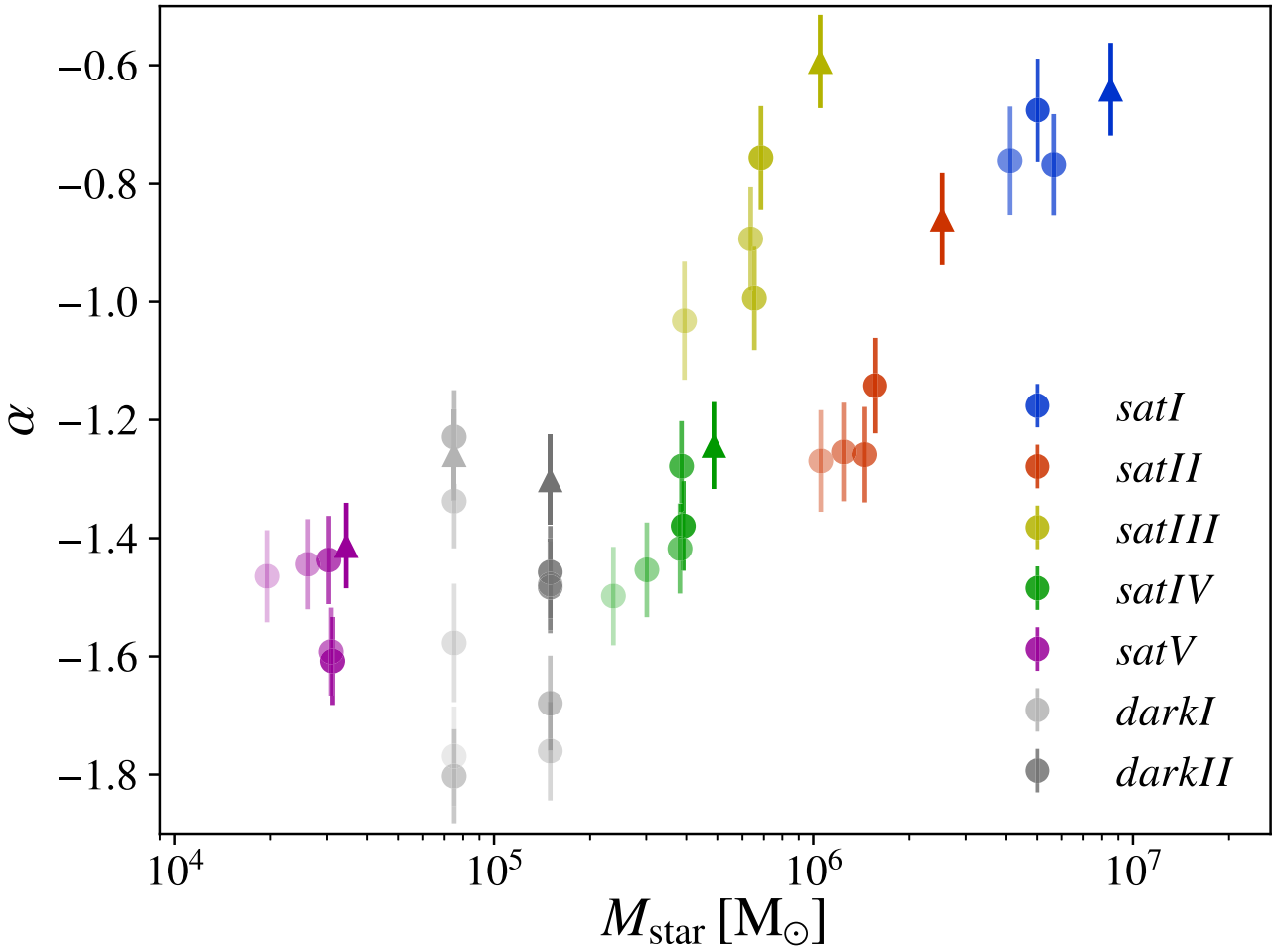

Figure 13. Inner logarithmic slope of the dark matter density profile α fitted between 1 per cent and 2 per cent of the virial radius as a function of stellar mass inside three 3D half-mass radii. Stars denote measurements at infall, while triangles denote the isolated simulations and filled circles the orbit runs at redshift $z = 0$. The more violent the orbit, the fainter is the colour.

Finally, we note that some satellites (especially *satI*) are left at $z = 0$ with practically no dark matter in their central region, where they are fully stellar dominated, resembling more an extended globular cluster than a dwarf galaxy, we plan to look more into this issue in a forthcoming paper.

4 DISCUSSION AND CONCLUSIONS

This work is the second of a series of papers in which we are trying to understand the formation and evolution of the smallest galaxies in the universe.

In the first paper (Paper I), we presented a series of 27 cosmological simulations of haloes in the mass range 5×10^8 to 10^{10} $M_\odot$, these simulations were run till $z = 1$ and aimed to describe the properties of satellite galaxies before accretion.

In this second paper, we used a subsample of these cosmological simulations as initial conditions for a series of binary hydrodynamical simulations (satellite + host) with the goal of understanding the effects of accretion and environment on satellite galaxies.

More specifically, we used a total of seven haloes (five luminous and two dark) with a virial mass in the range 4×10^9 to 10^{10} $M_\odot$. We modelled the central halo with an analytical potential of halo (NFW) plus disc (Miyamoto & Nagai), and we run the simulations from redshift one until redshift zero. We use five different orbits (plus a radial orbit) for a total of 42 simulations. Each galaxy is also evolved 'in isolation' meaning without the presence of the central halo for the same amount of time as our 'orbit' runs. We also add

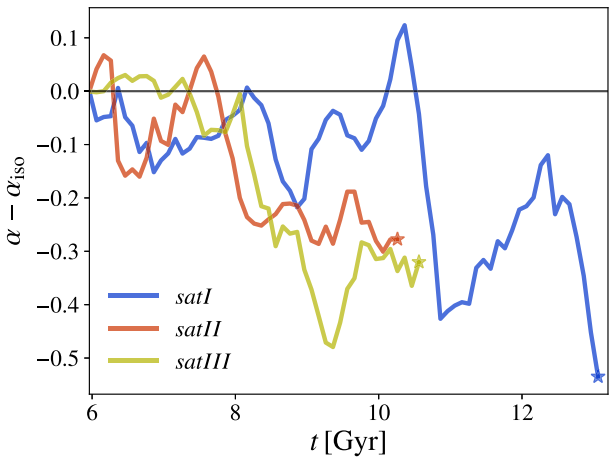

Figure 14. Time evolution of the deviation of α on *orbitIV* and *orbitV* from $\alpha_{\rm iso}$ (for the isolated runs) for *satI*, *satII* and *satIII*, respectively. The stars denote the time where there are less than 150 dark matter particles left inside a sphere of a radius of 1 per cent r_{200}.

Downloaded from https://academic.oup.com/mnras/article/472/3/3378/4093087 by guest on 10 January 2021

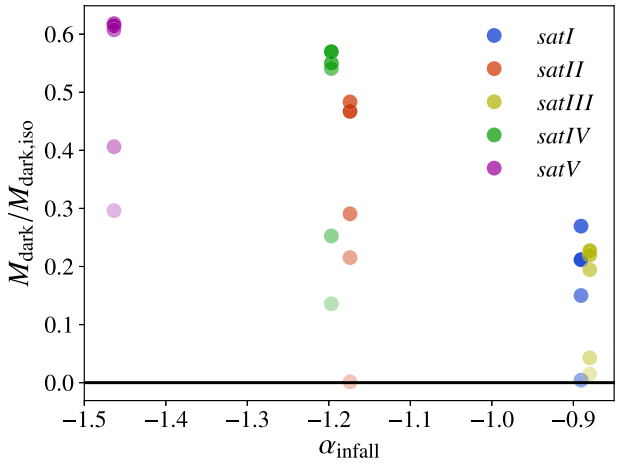

Figure 15. Dark matter mass enclosed in a constant sphere with a radius of three stellar half-mass radii at infall on the individual orbits compared to the isolated run as a function of the central dark matter density slope at infall $\alpha_{\rm infall}$.

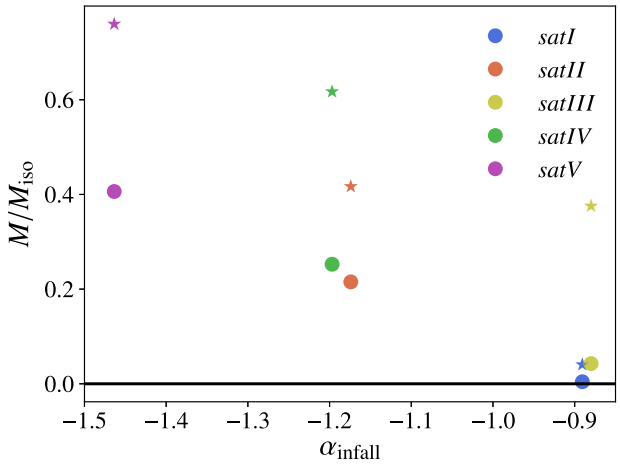

Figure 16. Dark matter (dots) and stellar (stars) mass enclosed in a constant sphere with a radius of three stellar half-mass radii at infall on *orbitIV* compared to the isolated run as a function of the central dark matter density slope at infall $\alpha_{\rm infall}$.

an analytical model for ram pressure and we test the results of our analytical potential against a live halo.

We find that our cosmological initial conditions differ from model (pre-cooked) galaxies in their kinematics: our galaxies, even before accretion do not have a well-defined rotating stellar disc and are dispersion supported, with an average value of v_φ/σ of 0.14, and as low as 0.04.

While orbiting around the central host, all galaxies lose a considerable fraction of their halo mass, as a consequence they drift away from the widely used abundance matching relations, due to a reshuffling of the mass rank order of the satellites. Only the more extreme orbits, with small pericentre distances, are effective in stripping the stellar component too, and the stripping is substantial only for our most massive (and extended) galaxies. Star formation is strongly suppressed after the infall (in comparison with the isolation run), this happens regardless of the presence or absence of ram pressure.

The environment has different effects on different scaling relations. In the stellar mass–metallicity plane, galaxies, even when they lose stellar mass, tend to keep an almost constant metallicity, due to the lack of strong metallicity gradients in the galaxy. In the size–velocity dispersion relation, galaxies move substantially in all directions, depending on their orbits and initial size. Galaxies tend to become more extended and to reduce their velocity dispersion (due to dark matter stripping). This explains the overall large observed scatter in the $r-\sigma$ plane.

Finally, the interaction with the host leads to a flattening of the stellar velocity dispersion profiles of the satellites, possibly due to the potential perturbation redistributing the stellar orbits into a more 'thermalized' system.

The dark matter component is also very strongly perturbed, first of all the removal of particles from the outer part of the haloes does not happen in an 'onion-like' fashion, with the external layers removed first. The whole density profile reacts to the accretion and even the most internal regions are affected by mass removal even if at a lower degree of the external ones. This implies an overall suppression of the circular velocity curves with respect to the isolation runs, even in the central part.

We find a correlation between the initial (at infall) inner dark matter density slope and the efficiency of mass removal and satellite survival which is in good agreement with previous studies. Cored satellites are less resilient to stripping and tidal forces and are more prone to lose a very large fraction of their dark matter mass (if not all of it) on orbits with close pericentre passages. Some cored satellites are so heavily stripped in their dark matter component that they end up being almost entirely stellar dominated within three stellar half-mass radii. Stars are also more easily stripped when embedded in a halo with a flat density profile, even though to a lower extent.

We witness a steepening of the central slope of the dark matter profile during accretion, with more extreme orbits ending up with the most cuspy dark matter profiles. Even profiles which initially (before accretion) have a dark matter density profile shallower than NFW (due to baryonic effects) evolve into cuspy profiles with slopes consistent with pure *N*-body simulations when set on orbits with small pericentre passages (7–20 kpc). Interestingly our dark haloes (without stars) also do steepen their profiles.

Overall our simulations seem to make a quite clear prediction of steep dark matter profiles for objects at the edge of galaxy formation, a prediction that, if falsified by observations, can force us to reconsider the collisionless and cold nature of dark matter.

ACKNOWLEDGEMENTS

This research was carried out on the High Performance Computing resources at New York University Abu Dhabi; on the THEO cluster of the Max-Planck-Institut für Astronomie and on the HYDRA clusters at the Rechenzentrum in Garching. TB and AVM acknowledge funding from the Deutsche Forschungsgemeinschaft via the SFB 881 programme 'The Milky Way System' (subproject A1 and A2). JF and AVM acknowledge funding and support through the graduate college *Astrophysics of cosmological probes of gravity* by Landesgraduiertenakademie Baden-Württemberg. JF and TB are members of the International Max-Planck Research School in Heidelberg. AO acknowledges support from the German Science Foundation (DFG) grant 1507011 847150-0. CP is supported by funding made available by ERC-StG/EDECS no. 279954.

REFERENCES

Aumer M., White S. D. M., Naab T., Scannapieco C., 2013, MNRAS, 434, 3142

Downloaded from https://academic.oup.com/mnras/article/472/3/3378/4093087 by guest on 10 January 2021

Blumenthal G. R., Faber S. M., Primack J. R., Rees M. J., 1984, Nature, 311, 517
Boylan-Kolchin M., Bullock J. S., Kaplinghat M., 2011, MNRAS, 415, L40
Bryan S. E., Mao S., Kay S. T., Schaye J., Dalla Vecchia C., Booth C. M., 2012, MNRAS, 422, 1863
Bullock J. S., Kolatt T. S., Sigad Y., Somerville R. S., Kravtsov A. V., Klypin A. A., Primack J. R., Dekel A., 2001, MNRAS, 321, 559
Caldwell N. et al., 2017, ApJ, 839, 20
Chan T. K., Kereš D., Oñorbe J., Hopkins P. F., Muratov A. L., Faucher-Giguère C.-A., Quataert E., 2015, MNRAS, 454, 2981
Chang J., Macciò A. V., Kang X., 2013, MNRAS, 431, 3533
Collins M. L. M. et al., 2013, ApJ, 768, 172
D'Onghia E., Besla G., Cox T. J., Hernquist L., 2009, Nature, 460, 605
Di Cintio A., Brook C. B., Macciò A. V., Stinson G. S., Knebe A., Dutton A. A., Wadsley J., 2014, MNRAS, 437, 415
Dutton A. A., Macciò A. V., 2014, MNRAS, 441, 3359
Dutton A. A., Macciò A. V., Frings J., Wang L., Stinson G. S., Penzo C., Kang X., 2016, MNRAS, 457, L74
Elbert O. D., Bullock J. S., Garrison-Kimmel S., Rocha M., Oñorbe J., Peter A. H. G., 2015, MNRAS, 453, 29
Flores R. A., Primack J. R., 1994, ApJ, 427, L1
Garrison-Kimmel S. et al., 2017, MNRAS, 471, 1709
Grand R. J. J. et al., 2017, MNRAS, 467, 179
Haardt F., Madau P., 2012, ApJ, 746, 125
Ho N. et al., 2012, ApJ, 758, 124
Hopkins P. F., Kereš D., Oñorbe J., Faucher-Giguère C.-A., Quataert E., Murray N., Bullock J. S., 2014, MNRAS, 445, 581
Kang X., van den Bosch F. C., 2008, ApJ, 676, L101
Kannan R., Stinson G. S., Macciò A. V., Brook C., Weinmann S. M., Wadsley J., Couchman H. M. P., 2014, MNRAS, 437, 3529
Kazantzidis S., Mayer L., Mastropietro C., Diemand J., Stadel J., Moore B., 2004a, ApJ, 608, 663
Kazantzidis S., Kravtsov A. V., Zentner A. R., Allgood B., Nagai D., Moore B., 2004b, ApJ, 611, L73
Kazantzidis S., Mayer L., Callegari S., Dotti M., Moustakas L. A., 2017, ApJ, 836, L13
Kirby E. N., Bullock J. S., Boylan-Kolchin M., Kaplinghat M., Cohen J. G., 2014, MNRAS, 439, 1015
Klypin A., Kravtsov A. V., Valenzuela O., Prada F., 1999, ApJ, 522, 82
Knollmann S. R., Knebe A., 2011, Astrophysics Source Code Library, record ascl:1102.009
Komatsu E. et al., 2011, ApJS, 192, 18
Łokas E. L., Kazantzidis S., Klimentowski J., Mayer L., Callegari S., 2010, ApJ, 708, 1032
Macciò A. V., Paduroiu S., Anderhalden D., Schneider A., Moore B., 2012a, MNRAS, 424, 1105
Macciò A. V., Stinson G., Brook C. B., Wadsley J., Couchman H. M. P., Shen S., Gibson B. K., Quinn T., 2012b, ApJ, 744, L9
Macciò A. V., Mainini R., Penzo C., Bonometto S. A., 2015, MNRAS, 453, 1371
Macciò A. V., Frings J., Buck T., Penzo C., Dutton A. A., Blank M., Obreja A., 2017, MNRAS, preprint (arXiv:1707.01106) (Paper I)
Marinacci F., Pakmor R., Springel V., 2014, MNRAS, 437, 1750
Martin N. F. et al., 2014, ApJ, 793, L14
Mayer L., Mastropietro C., Wadsley J., Stadel J., Moore B., 2006, MNRAS, 369, 1021
Miyamoto M., Nagai R., 1975, PASJ, 27, 533
Moore B., 1994, Nature, 370, 629
Moster B. P., Naab T., White S. D. M., 2013, MNRAS, 428, 3121
Moster B. P., Macciò A. V., Somerville R. S., 2014, MNRAS, 437, 1027
Munshi F., Brooks A. M., Applebaum E., Weisz D. R., Governato F., Quinn T. R., 2017, preprint (arXiv:1705.06286)
Navarro J. F., Frenk C. S., White S. D. M., 1996, ApJ, 462, 563
Oh S.-H. et al., 2015, AJ, 149, 180
Oñorbe J., Boylan-Kolchin M., Bullock J. S., Hopkins P. F., Kereš D., Faucher-Giguère C.-A., Quataert E., Murray N., 2015, MNRAS, 454, 2092
Peebles P. J. E., 1984, ApJ, 277, 470
Peñarrubia J., Benson A. J., Walker M. G., Gilmore G., McConnachie A. W., Mayer L., 2010, MNRAS, 406, 1290
Penzo C., Macciò A. V., Casarini L., Stinson G. S., Wadsley J., 2014, MNRAS, 442, 176
Perlmutter S. et al., 1999, ApJ, 517, 565
Pontzen A., Governato F., 2012, MNRAS, 421, 3464
Power C., Navarro J. F., Jenkins A., Frenk C. S., White S. D. M., Springel V., Stadel J., Quinn T., 2003, MNRAS, 338, 14
Read J. I., Gilmore G., 2005, MNRAS, 356, 107
Riess A. G. et al., 1998, AJ, 116, 1009
Sawala T. et al., 2016, MNRAS, 457, 1931
Schaye J. et al., 2015, MNRAS, 446, 521
Shen S., Wadsley J., Stinson G., 2010, MNRAS, 407, 1581
Springel V., Di Matteo T., Hernquist L., 2005, MNRAS, 361, 776
Stinson G., Seth A., Katz N., Wadsley J., Governato F., Quinn T., 2006, MNRAS, 373, 1074
Stinson G. S., Brook C., Macciò A. V., Wadsley J., Quinn T. R., Couchman H. M. P., 2013, MNRAS, 428, 129
Tollerud E. J. et al., 2012, ApJ, 752, 45
Tollerud E. J., Geha M. C., Vargas L. C., Bullock J. S., 2013, ApJ, 768, 50
Tollet E. et al., 2016, MNRAS, 456, 3542
Vogelsberger M. et al., 2014a, MNRAS, 444, 1518
Vogelsberger M., Zavala J., Simpson C., Jenkins A., 2014b, MNRAS, 444, 3684
Wadsley J. W., Stadel J., Quinn T., 2004, Nature, 9, 137
Walker M. G., Mateo M., Olszewski E. W., Peñarrubia J., Wyn Evans N., Gilmore G., 2009, ApJ, 704, 1274
Wang L., Dutton A. A., Stinson G. S., Macciò A. V., Penzo C., Kang X., Keller B. W., Wadsley J., 2015, MNRAS, 454, 83
Wetzel A. R., Hopkins P. F., Kim J.-h., Faucher-Giguère C.-A., Kereš D., Quataert E., 2016, ApJ, 827, L23
Wheeler C. et al., 2017, MNRAS, 465, 2420
White S. D. M., Rees M. J., 1978, MNRAS, 183, 341
Wolf J., Martinez G. D., Bullock J. S., Kaplinghat M., Geha M., Muñoz R. R., Simon J. D., Avedo F. F., 2010, MNRAS, 406, 1220

This paper has been typeset from a TEX/LATEX file prepared by the author.

Downloaded from https://academic.oup.com/mnras/article/472/3/3378/4093087 by guest on 10 January 2021